Journal of Quantitative Spectroscopy & Radiative Transfer 328 (2024) 109172

Contents lists available at ScienceDirect

Journal of Quantitative Spectroscopy and Radiative Transfer

journal homepage: www.elsevier.com/locate/jqsrt

Continuum absorption in pure N_2 gas and in its mixture with Ar

E.A. Serov [a], T.A. Galanina [a], A.O. Koroleva [a], D.S. Makarov [a], I.S. Amerkhanov [a], M.A. Koshelev [a], M.Yu. Tretyakov [a,*], D.N. Chistikov [b,c,d], A.A. Finenko [c,a,d], A.A. Vigasin [b,a]

[a] Federal Research Center A. V. Gaponov-Grekhov Institute of Applied Physics of the Russian Academy of Sciences, 46 Ulyanov Street, Nizhny Novgorod 603950, Russia
[b] A. M. Obukhov Institute of Atmospheric Physics, Russian Academy of Sciences, 3 Pyzhevsky Per., Moscow 119017, Russia
[c] Department of Chemistry, Lomonosov Moscow State University, GSP-1, 1-3 Leninskiye Gory, Moscow 119991, Russia
[d] Institute of Quantum Physics, Irkutsk National Research Technical University, 83 Lermontov str., Irkutsk 664074, Russia

ARTICLE INFO

Keywords:
Bimolecular absorption
Collision-induced absorption
subTHz range
Broadband resonator spectroscopy
Classical trajectory-based simulation
Nitrogen-rich atmospheres
Absorption model

ABSTRACT

The N_2–N_2 and N_2–Ar continuum absorption spectra are calculated using the classical trajectory-based simulation (CTS). The spectra obtained are validated by new measurements in the subTHz spectral range along with the previously reported data in the far infrared. A novelty of our approach consists in the use of the CTS method to simulate both the fundamental nitrogen absorption band and the rototranslational band in N_2–Ar, i.e., we succeeded to step beyond the conventionally used approximation of the only rigid monomers. This extension of the theory made it possible, in particular, to demonstrate the validity of the rigid monomer assumption for the CTS simulation of the rototranslational N_2–Ar band. The broadband spectra within 77–354 GHz were measured using the resonator spectrometer at temperatures of 278–333 K and pressures of 900–1600 Torr. A minor underestimation of the calculated absorption by 3.7% and 5% is shown for the N_2–N_2 and N_2–Ar system, respectively. On the basis of the obtained data, a new analytical model is developed for the N_2–N_2 absorption in the subTHz range, which can be used in radiation propagation codes for the Earth, Titan, or other nitrogen-rich atmospheres. The advantage of the model proposed here over those previously published is discussed.

1. Introduction

The molecular composition of the presently known planetary atmospheres is by far dominated by rather simple, symmetrical species. Inversion symmetry precludes such molecules from having a permanent electric dipole, thus making the dominant atmospheric constituents low absorbing at least in the long-wave infrared and microwave spectral ranges. Provided the absorption of polar atmospheric admixtures can be neglected, the opacity of the atmosphere can only be driven by intermolecular forces which give rise to temporal perturbation of the charge distribution in individual symmetrical molecules interacting with each other. Because of this, the radiative budget of giant planets is largely determined by the so-called collision-induced absorption (CIA) in the hydrogen-containing molecular pairs [1]. The radiative budget of the nitrogen-dominated Earth's atmosphere are virtually insensitive to collision-induced effects because of omnipresent and much stronger water-vapor resonant and continuum absorption. However, the supermolecular water-nitrogen absorption is a significant part of the water vapor continuum in various spectral ranges [2]. Moreover, pure nitrogen CIA clearly manifests itself in the stratosphere [3] where it is less concealed by strong water vapor absorption in comparison with the near-surface layers. A striking example of the nitrogen-born radiative effect relates to the Titan atmosphere, in which both N_2–N_2 and N_2–CH_4 CIA determine the planetary thermal radiance [4].

A detailed laboratory study of continuum microwave absorption in pure nitrogen was undertaken in a number of works (see, e.g., [5,6] and references therein). The contemporary theoretical approaches, which were used to simulate CIA far-infrared spectra of N_2–N_2 and N_2–Ar, include the quantum theory (QT) [7], the classical molecular dynamics simulation (CMDS) [8], and the semiclassical trajectory simulation (CTS) [9], all based on the *ab initio* predictions of both the intermolecular interaction potential and induced-dipole moment surfaces under the assumption of rigid monomers. In all cases, the theoretical description of induced spectra is in satisfactory agreement with the available observations. It is worth mentioning that both the QT and

* Corresponding author.
E-mail addresses: serov@ipfran.ru (E.A. Serov), odintsova@ipfran.ru (T.A. Galanina), koral@ipfran.ru (A.O. Koroleva), dmak@ipfran.ru (D.S. Makarov), i.amerhanov@ipfran.ru (I.S. Amerkhanov), koma@ipfran.ru (M.A. Koshelev), trt@ipfran.ru (M.Yu. Tretyakov), danichist@yandex.ru (D.N. Chistikov), artfin@mail.ru (A.A. Finenko), vigasin@ifaran.ru (A.A. Vigasin).

https://doi.org/10.1016/j.jqsrt.2024.109172
Received 18 June 2024; Received in revised form 23 August 2024; Accepted 23 August 2024
Available online 26 August 2024

CMDS methods require huge computational resources; the spectrum of anisotropically interacting N_2–N_2, for instance, was characterized in [7] by eight points only on the frequency scale. In contrast, the CTS approach is not as processor-time-consuming; it allows one to simulate easily the N_2–N_2 rototranslational CIA spectra [9] in a wide range of temperatures. Moreover, this method is fairly applicable to simulation of the spectra of true bound dimers, such as CO_2–Ar, revealing a significant temperature variation of the dimer band shape [10].

The present paper aims at detailed experimental and theoretical characterization of the millimeter-submillimeter wave absorption in the N_2–N_2 and N_2–Ar pairs. The results of the new measurements are reported for the 77–120, 156–257, and 247–354 GHz spectral ranges in the case of pure nitrogen at temperatures within about ±20 degrees around 296 K, and for 156–257 GHz in N_2–Ar at room temperature. These data, together with the experimental data from our previous study [6], are then compared with the simulated results obtained using the trajectory-based method. A new practical model is then suggested that may be used to simulate the radiative transfer of sub-terahertz (subTHz) radiation in the nitrogen-rich atmosphere. We also report some preliminary results of our trajectory-based simulation of the nitrogen fundamental absorption band in the N_2–Ar mixture. This simulation relies on a complete, full-dimensional potential energy surface (PES) and an induced dipole surface (IDS), which were constructed from the fitting of an *ab initio* set of discrete values using the neural network PIP-NN algorithm. The obtained band shape was then compared with the available laboratory data.

The paper is organized as follows. The measurement details, the continuum spectra retrieval, and the development of the new N_2–N_2 absorption model are given in Section 2. The theoretical calculations of the N_2–Ar spectra and results of their validation by the empirical data are presented in Section 3. Section 4 is devoted to the comparison of the new N_2–N_2 model with those previously known, taking the calculation of the Titan's atmospheric brightness temperature as an example.

2. Details of the experiment and continuum spectra analysis

2.1. Similar features of the N_2–N_2 and N_2–Ar continua

Let us consider the virial equation of state for a gas:

$$\frac{pV_m}{RT} = 1 + \frac{B(T)}{V_m} + \frac{C(T)}{V_m^2} + \cdots, \tag{1}$$

where p, T, and V_m are, respectively, the gas pressure, temperature, and molar volume, R is the gas constant, and $B(T)$ and $C(T)$ are the second and third virial coefficients, which arise due to intermolecular interactions, so that $B(T)$ is determined by the pairwise forces only, whereas $C(T)$ contains contributions both from molecular triples and pairs. At temperatures ranging from 100 to 320 K and a pressure of about 1 atm (which is typical for Earth's and Titan's atmospheres, the ratio of the second to the third term $(B(T)/V_m)/(C(T)/V_m^2)$ in the Eq. (1) ranges from 20 to 350 for nitrogen and from 300 to 600 for argon. This can be considered an indication of pairwise interactions being dominant in relevant pure gases and their mixtures. Moreover, the ratio of the molecular mean free path to the effective collisional cross-section radius (which is supposed to correlate with the effective size of a molecule) can be evaluated in the assumption of rigid spheres within the gas kinetic theory using the information about pressure broadening of quadrupole pure rotational transitions in nitrogen from the HITRAN database [11]. This ratio ranges from 25 up to 200 at 2 atmospheres (the maximum pressure used in our experiments) and temperatures within 100–400 K, thus confirming the validity of our consideration constrained by the use of the binary approximation only.

The assumption that our measured absorption spectra have a bimolecular nature allows considering them as being proportional to the pressure squared in pure gas or to the product of partial pressures in the gas mixture. Under our explored conditions, the absorption in pure argon is negligible. Thus, the measured absorption coefficient α is due to the absorption caused by the combined effect of the interaction of N_2 molecules either with other N_2 molecules (self-continuum) or with Ar atoms (foreign continuum):

$$\begin{aligned}\alpha(f, p_{N_2}, p_{Ar}, T) &= \alpha_{N_2-N_2}(f, p_{N_2}, T) + \alpha_{N_2-Ar}(f, p_{N_2}, p_{Ar}, T) = \\ &= C_{N_2-N_2}(f, T) p_{N_2}^2 + C_{N_2-Ar}(f, T) p_{N_2} p_{Ar},\end{aligned} \tag{2}$$

where f is the frequency in GHz, p_{N_2} and p_{Ar} are the nitrogen and argon partial pressures, and $C_{N_2-N_2}(f,T)$ and $C_{N_2-Ar}(f,T)$ are the pressure-normalized continuum coefficients. In pure N_2, the second term vanishes.

The dependence of the continuum coefficients on the frequency and temperature is different in various frequency ranges. However, for atmospheric applications, these dependencies are conventionally approximated by simple empirical models. For example, in the millimeter and submillimeter wavelength ranges a power-law dependence can be used [5,12]:

$$C_{N_2-N_2}(f,T) = S_{N_2-N_2}(f,T_0) f^2 \left(\frac{T_0}{T}\right)^{n_{N_2-N_2}} \tag{3}$$

where $S_{N_2-N_2}(f,T_0)$ is *the reduced spectral function* (hereafter called just the spectral function for brevity) corresponding to N_2–N_2 continuum, $n_{N_2-N_2}$ is the temperature exponent, and $T_0 = 300$ K. A more physically justified formula for the temperature dependence of bimolecular absorption was suggested in [13]:

$$C_{X-Y}(f,T) \sim C_{0,X-Y}(f) T^{-n} \left(\exp\left(\frac{D_0}{k_B T}\right) - \left(1 + \frac{D_0}{k_B T}\right)\right) \tag{4}$$

where $C_{0,X-Y}(f)$ is the temperature-independent part of bimolecular absorption coefficient, k_B is the Boltzmann constant, D_0 is the dissociation energy of the molecular complex X–Y, $n = 5/2 - (m + \chi)$, and $\chi = -1$ in case $h\nu \ll k_B T$ (microwave continua) or $\chi = 0$ in case $h\nu \gg k_B T$ (infrared continua). The value of m depends on the number of rotational and classical vibrational (intermolecular) degrees of freedom characteristic of the complex or its monomeric progenitors (see [13] for details). In the case of N_2–N_2 bimolecular absorption, the value of m can be estimated as being in the range from 0.5 to 1, leading consequently to n between 2 and 4.

2.2. Experimental details

All spectra were recorded using a resonator spectrometer [14]. The experimental method is based on measuring a variation in the resonance response width of a high–Q Fabry–Perot resonator with and without the studied gas inside. Pure gases with the declared purity exceeding 99.99% were provided by a local supplier. 625B MKS Baratron and CCR 361 Pfeiffer vacuum gauges with relative uncertainties of 0.25 and 0.2% and maximal pressures of 2000 and 1000 Torr, respectively, were used. The temperature of the gas and the cavity mirrors was permanently monitored using standard PT–100 sensors with an uncertainty of 0.2 K. For cavity heating and cooling, we used a Julabo FP-5 thermostat. The absorption spectra of nitrogen were recorded in three spectral sub-bands: 77–120, 156–257, and 247–354 GHz, corresponding to the three different backward wave oscillators (BWOs) used as radiation sources. Two types of detectors were used. At frequencies below 260 GHz, commercial detectors based on low-barrier planar Schottky diodes were employed, whereas an InSb bolometer cooled by liquid helium was used at higher frequencies. The spectra of the nitrogen-argon mixture were studied only in the 156–257 GHz range. The resonator intrinsic losses (the spectrum baseline) were measured when the cavity was filled with argon both for N_2–N_2 and N_2–Ar mixture. Argon pressure was adjusted so that the optical path length inside the cavity (defined as the length of the cavity multiplied by refractive index of the gas) was the same as for the studied gas. After the losses of the gas-filled cavity were measured and

Table 1
Experimental conditions.

#	Frequency range, GHz	Temperature, K	p, Torr	p_{Ar}, Torr	Number of spectra
1	77–120	278	1506	0	4
2	77–120	296	1009	0	3
3	77–120	296	1475	0	3
4	77–120	317	1430	0	3
5	156–257	279	1001	0	4
6	156–257	279	1275	0	2
7	156–257	279	1284	0	4
8	156–257	279	1509	0	4
9	156–257	297	1515	0	11
10	156–257	317	1001	0	3
11	156–257	317	1284	0	4
12	156–257	317	1510	0	4
13	156–257	333	1518	0	3
14	156–257	297	1583	1079	4
15	156–257	297	1569	968	4
16	156–257	297	1516	762	4
17	247–354	297	923	0	2
18	247–354	300	1439	0	5

the gas spectrum was retrieved, we repeated the whole procedure 2–4 times at different distances between the cavity and the radiation source in order to average the spectra and minimize the effect of parasitic reflections in the waveguides (see [14] for details). The temperature of the cavity mirrors slightly drifted during the measurement, which influenced the intrinsic losses of the resonator. This effect amounts to several percents of the measured gas absorption and was taken into account by the calculation of the temperature variations of intrinsic resonator losses using the data from [15]. The experimental conditions of the recorded spectra are listed in Table 1.

The following procedure for spectral functions data reduction and analysis was slightly different for pure nitrogen and nitrogen-argon mixture. First, all the N_2–N_2 spectra corresponding to the same temperature and the same frequency range were normalized by pressure squared and compared to each other (Fig. 1). The discrepancies between spectra are much smaller than the standard deviation of experimental noise, confirming the correspondence of the obtained data to Eq. (2). As expected, the highest pressure spectrum points have the minimal scatter because the relevant signal-to-noise ratio is maximal in the series.

In several experimental spectra, an H_2O line near 183 GHz is observed. An example of its manifestation in the case of the N_2–Ar mixture is shown in Fig. 3. The line originates from trace water vapor, which is a practically unavoidable impurity in gas samples. The water vapor partial pressure was determined spectroscopically from the known line intensity and did not exceed 3 mTorr. The corresponding contribution of the water-vapor-related continua was calculated and taken into account using data from [16,17] (assuming the quadratic continuum frequency dependence). The quadratic frequency dependence of these water-vapor-related continua in the range under study was assumed. These corrections did not exceed 1% of the measured absorption.

At the next step, all pressure-normalized spectra were averaged with weights proportional to the squared standard deviation of the experimental points from the f^2 dependence. This dependence is good enough to model the continuum in every frequency sub-band, while in the whole 77–354 GHz range under study, a more accurate model should be used, as will be shown in the following subsection. As a result, we obtained the averaged spectra $C_{N_2-N_2}(f,T)$ and the spectral function $S_{N_2-N_2}(f,T)$ corresponding to each temperature. The obtained spectral functions are shown in Fig. 2. Results of our previous study [6] of the N_2–N_2 continuum obtained under close conditions are also shown for comparison, demonstrating their similarity and agreement with the new data. Each experimental point in Fig. 2 was obtained by taking the average 8 neighboring points from the initial spectrum in order to improve the clarity of the figure.

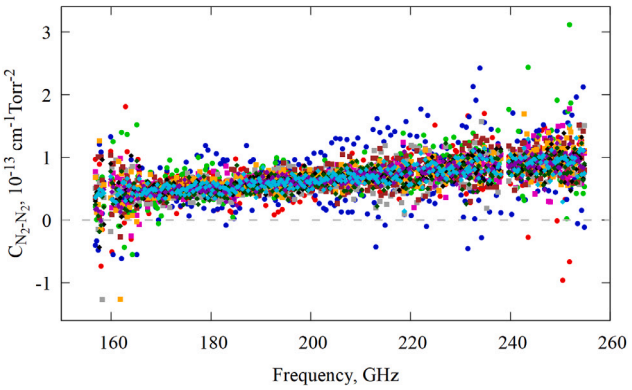

Fig. 1. Experimental absorption spectra of N_2 normalized by pressure squared at T = 317 K. Circles, squares and diamonds correspond to 1001, 1284 and 1510 Torr, respectively. Different experimental recordings are shown by different colors.

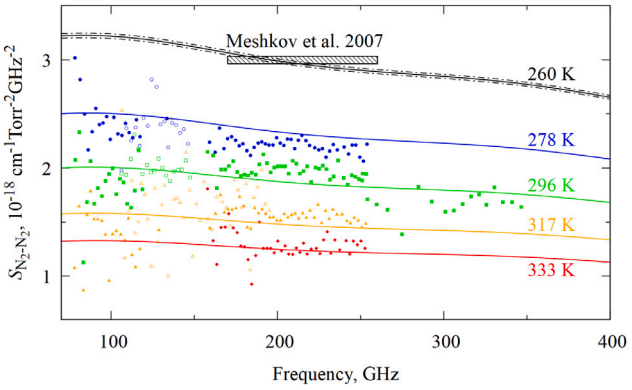

Fig. 2. Spectral functions of N_2–N_2 at four temperatures. Blue circles, green squares, orange triangles and red diamonds shows the experimental data for 278, 296, 317 and 333 K, respectively. Solid curves are for the model fitted simultaneously to all the data, and the dashed lines are for its uncertainty interval. The results of our previous study [6] (recalculated from 280, 297 and 310 K using the temperature exponent determined in this work) are shown by open symbols of the corresponding type and color. The rectangular in the upper part of the figure shows the spectral range and uncertainty interval of the averaged experimental results from [5] (see text for details).

Bimolecular absorption by the N_2–Ar system was determined from the spectra of N_2 with Ar mixture after subtracting the N_2–N_2 component (Eq. (2)). The smooth approximating function presented in the next subsection was used for the subtraction. Note that the N_2–N_2 contribution constitutes about 50% of the total mixture absorption. First, as in the case of pure nitrogen, the retrieved N_2–Ar absorption was normalized by the product of the partial pressures of interacting species to obtain the ensemble of $C_{N_2-Ar}(f)$ values. The pressure-normalized spectra coincide with each other within the experimental noise level and can thus be averaged to improve the signal-to-noise ratio (Fig. 3). The contribution of trace water vapor was evaluated using data from [17] and subtracted from the averaged spectrum.

2.3. N_2–N_2 experimental data interpretation

The experimental data on the N_2–N_2 and N_2–Ar spectral functions were interpreted as bimolecular absorption in these collisional systems, which was calculated using the CTS method without recourse to any empirical parameters as described in detail in [9,18]. The main results of these calculations for N_2–N_2 are included in the collision-induced absorption (CIA) section of the HITRAN database [11].

For N_2–N_2 experimental data processing, we used an empirical model of the spectral function which was optimized to the theoretical

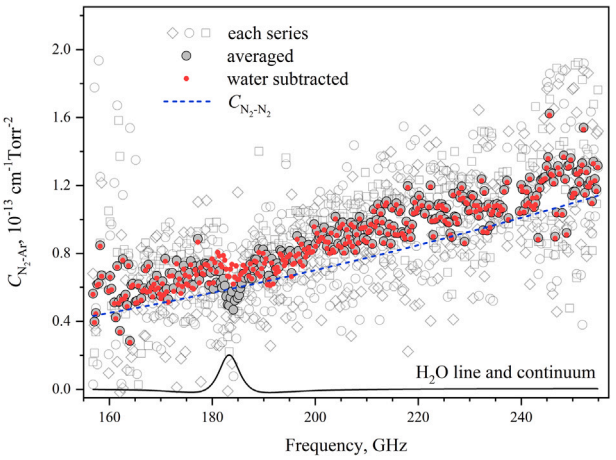

Fig. 3. Measured normalized absorption spectra $C_{N_2-Ar}(f)$ (open gray symbols) and their average (filled gray circles). The black curve corresponds to the calculated water vapor absorption. The blue dashed line is for $C_{N_2-N_2}(f)$, which is given here for comparison. The red circles are for the measured absorption, cleaned from the water contribution.

CIA spectra in the frequency range 0–1.2 THz for two temperature intervals, 70–200 and 200–330 K. To develop the model, we took into account that N_2–N_2 absorption within the considered range of parameters (i) has a frequency dependence close to f^2, and (ii) its temperature dependence is close to Eq. (4). Based on these assumptions, the following model for the reduced spectral function was used:

$$S_{N_2-N_2}(f,T) = S_0(f)\left(\frac{T_0}{T}\right)^{n(f,T)}\left\{\frac{\exp\left(D_0/k_BT\right)-\left(1+D_0/k_BT\right)}{\exp\left(D_0/k_BT_0\right)-\left(1+D_0/k_BT_0\right)}\right\}, \tag{5}$$

where $D_0 = 108$ cm^{-1} [7], $T_0 = 300$ K, the temperature exponent n is a function of the frequency and the temperature

$$n(f,T) = n_0(f) + b(f)\ln\left(\frac{T_0}{T}\right) \tag{6}$$

with $n_0(f) = \sum_{j=1}^{3} a_j f^j$, $b(f) = \sum_{j=1}^{3} b_j f^j$. The frequency dependence of the spectral function is given by

$$S_0(f) = \frac{A_0}{2}\left(1 + A_1\frac{1+\frac{A_2}{1+\left(\frac{f-F_3}{F_4}\right)^2}}{1+\left(\frac{f-F_1}{F_2}\right)^2} + A_3\exp\left(-\left(\frac{f}{F_5}-1\right)^2\right)\right). \tag{7}$$

The numerical coefficients of the model as determined for the two temperature intervals 70–200 and 200–330 K are reported in Table 2. The deviation of the calculated spectral points from the fitted function is less than 2.9% and 1.7% in the low and high temperature intervals, respectively. The correspondence of the model to the calculated spectra is shown in Fig. 4. Note that the modern version of the atmospheric Millimeter-wave Propagation model (MPM, see [19] and the MWRnet website [20]) employs a simpler function describing the dry air absorption (where nitrogen is the dominating contributor), which can be obtained from Eq. (7) with $A_1 = 1$, $A_2 = A_3 = F_1 = 0$, and $F_2 = 450$ GHz. A comparison of this simplified model with the trajectory-based calculated spectrum (Fig. 4) shows that it does not reproduce all features of the absorption, such as the local maxima near 100 GHz and the inflection points.

Table 2
Numerical parameters of the N_2–N_2 spectral function model Eqs. ((5)–(7)) for two temperature intervals.

Parameter	Units	70–200 K	200–330 K
A_0	cm^{-1}Torr^{-2}GHz^{-2}	1.164×10^{-18}	1.678×10^{-18}
A_1	–	2.159	1.046
A_2	–	−0.1857	0.1640
A_3	–	0.2676	0.1447
F_1	GHz	217	28
F_2	GHz	623	587
F_3	GHz	570	360
F_4	GHz	208	131
F_5	GHz	86	95
a_0	–	1.3828	1.4363
a_1	GHz^{-1}	-8.044×10^{-4}	-5.280×10^{-4}
a_2	GHz^{-2}	8.019×10^{-8}	1.0126×10^{-7}
a_3	GHz^{-3}	6.2784×10^{-10}	2.286×10^{-10}
b_0	–	0.1451	0.07907
b_1	GHz^{-1}	-3.899×10^{-4}	-5.412×10^{-4}
b_2	GHz^{-2}	1.599×10^{-6}	1.2741×10^{-6}
b_3	GHz^{-3}	-1.202×10^{-9}	-6.689×10^{-10}

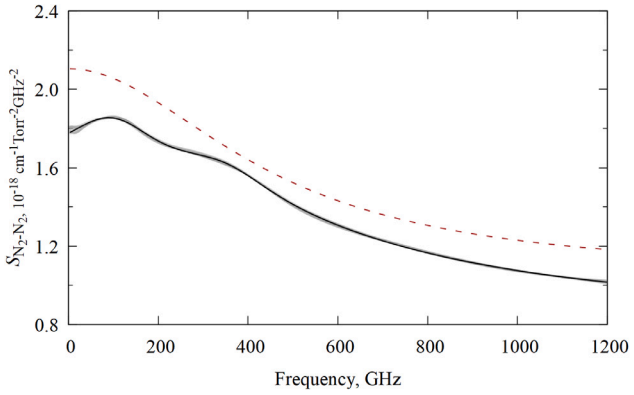

Fig. 4. N_2–N_2 spectral functions obtained by the CTS method for the 200–330 K interval and recalculated to 300 K (gray circles) and their approximation by the model according to Eqs. (5)–(7) (solid black line). The dashed line is the function from the current MPM version [20] recalculated to pure nitrogen (see Section 4 for details).

The high temperature spectral function was optimized simultaneously to all experimental data (Table 1 and data from [6]) using its amplitude as the only variable parameter. The result is shown in Fig. 2 by the solid curves demonstrating agreement of the frequency and temperature dependencies of the spectrum obtained experimentally and calculated by the CTS method, thus validating the results of the CTS calculations. Almost perfect coincidence of the fitted model with the most accurate previous measurements [5] is shown in the upper part of Fig. 2 (the continuum coefficients and their uncertainties reported in Eq. (16) from [5] retrieved from the very large experimental dataset obtained within 170–260 GHz at 229–323 K are used for the spectral function value calculation at 260 K). The achieved agreement justifies the use of the theoretical temperature dependence Eq. (6) for the N_2–N_2 spectrum modeling. The temperature exponent $n(f,T)$ of the N_2–N_2 absorption model obtained in this way is ranging within 3.1 and 3.6, which is in perfect agreement with the theoretical expectation given by Eq. (4). The optimized amplitude of the model was found to be only 3.7% larger than its initial value also confirming the very high quality of the CTS data. For the high accuracy modeling we recommend applying the 1.037 multiplier to the A_0 parameter of the model, at least for the 200–330 K interval. We assess the relative uncertainty of the model as about 0.7% including the statistical uncertainty of the fit (which is low due to the very large number and good repeatability of experimental points within a wide range of pressures, temperatures and frequencies and the only one adjustable parameter) and the stated uncertainties of the pressure and temperature sensors.

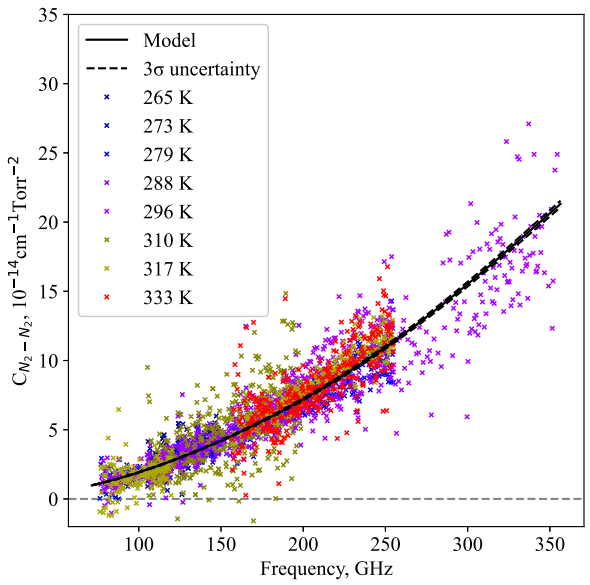

Fig. 5. Experimental data on N_2–N_2 recalculated to 300 K (points) and the absorption model fitted to them (Eqs. (3)–(7)) (solid line). The dashed lines show the 3σ statistical uncertainty interval of the model.

To demonstrate further the consistency of the experimental data set and the absorption model, we recalculated all measurement data to 300 K and compared them with the model. The result is shown in Fig. 5.

3. Trajectory-based simulation of the rototranslational and the fundamental N_2 CIA bands assuming fully flexible N_2−Ar

The trajectory-based simulation for N_2−Ar CIA, which we report here, represents an important extension of the general methodology that was illustrated in [10,21] for the cases of the CO_2−Ar and CO_2−CO_2 CIA. To the best of our knowledge, the CTS method for modeling CIA band shapes has never been employed before when the interacting moieties are considered flexible. One of the hurdles for such a simulation is conditioned by the need to possess a potential energy surface and the induced dipole surface encompassing both the intra- and intermolecular degrees of freedom. Section 3.1 explains the construction of the necessary PES and IDS. In Section 3.2, the dynamical equations governing the time evolution of the bimolecular complex are examined. The changes made to the Monte Carlo scheme for computing the dipole time-correlation function with respect to what was detailed earlier in [10] are covered in Section 3.3.

3.1. Potential energy and induced dipole surfaces

The full-dimensional representation of the two-body components of the dimer energy and dipole is achieved through the application of the permutationally-invariant polynomial neural network (PIP-NN) approach. In this method, a subset of polynomials in interatomic distances (or functions thereof) is specifically prepared to characterize the fundamental properties of the surfaces and is subsequently fed into a fully-connected neural network [22]. A brief recapitulation of the techniques regarding constructing PIP-NN IDS is given here, whereas Ref. [18] discusses in detail our approach to constructing PIP-NN PESs for weakly bound systems.

The permutationally invariant polynomials are constructed using transformed interatomic distances τ_{ij} as variables. The functional form of the transformed internuclear distances is set to the Morse function for the intramolecular degrees of freedom and the mixed Morse-polynomial function for the intermolecular ones. During the PIP-NN model's training, the interatomic distance parameters remain unchanged; only the polynomial weights are tuned. The MSA software [23,24] is utilized to construct the polynomials of the invariant basis. The disconnected terms are then eliminated [25] in order to improve the fit quality at large intermolecular separations.

The dipole moment is represented in the following form

$$\hat{\boldsymbol{\mu}} = \sum_{i=1}^{N} q_i \mathbf{r}_i, \tag{8}$$

where q_i is the effective charge of i-th center and $\mathbf{r}_i$ is the corresponding position vector. The effective charges are scalar quantities that depend on interatomic distances and must adhere to certain covariant properties resulting from the fact that the dipole moment is invariant under permutations of like atoms. Namely, the effective charge of Ar is invariant under the permutation of N1 and N2. By contrast, the effective charges of permuted centers must interchange. A charge that is transformed in a covariant manner with respect to permutations of like centers is invariant under the operations of the modified permutational group corresponding to the virtual atomic system, where the considered atom is labeled uniquely [26]. Lastly, we should address the electroneutrality of the constructed model. Within this representation, the constraint on the sum of effective charges could be included in the loss function:

$$\mathcal{L} = \frac{1}{M}\sum_{i=1}^{M} w_i \left(\hat{\boldsymbol{\mu}} - \boldsymbol{\mu}_i\right)^{\top}\left(\hat{\boldsymbol{\mu}} - \boldsymbol{\mu}_i\right) + \frac{1}{M}\sum_{i=1}^{M}\kappa\left(\sum_{j=1}^{N} q_j\right)^2, \tag{9}$$

where M is the number of configurations within the dataset and κ (set to 10^5) is the hyperparameter relating to the strictness of the electroneutrality criterion.

In addition to the effective charges centered on atoms, we also place two additional centers denoted with X on a line perpendicular to the N–N bond, so that N_2X_2 forms a square in the N–N–Ar plane. From the symmetry standpoint, the additional centers X belong to the same type, so overall the set of centers possesses the "221" permutational symmetry. The improved accuracy of this model over a 3-center model is likely due to the fact that the square arrangement of charges provides a better approximation for the dipole's dominant quadrupole-induced component. For each type of the center, we construct the corresponding polynomial basis, which is fed into the neural-network model to produce the values of the respective effective charges.

The dipole moment was calculated in the MOLPRO package [27] at CCSD(T)-F12a/aug-cc-pVTZ level of theory using the finite-field approach. The obtained values were corrected for BSSE using the Boys–Bernardi compensation scheme [28]. A grid of configurations was constructed using Jacobi coordinates, namely, using the distance between moieties' centers of mass, the angle enclosed between the molecular axis of N_2 and the intermolecular vector, and N_2's bond length. For radial variables, a grid consisting of 31 intermolecular distance values in the range from 4.5 to 30 a.u. was used, as well as 21 N_2 bond lengths ranging from 1.798 to 2.358 a.u., and the 13-point Gauss–Legendre grid, of which only 7 points are symmetrically unique, was employed for the angular coordinate. Note that the equilibrium length N_2 is 2.0785 a.u. [29]. The range of variation of the N_2 bond length was chosen to cover the monomer vibrational excitations up to 3000 cm^{-1}. In total, dipole moment calculations were conducted for $M = 31\,(\text{radial grid}) \times 21\,(\text{bond length grid}) \times 7\,(\text{angular grid}) = 4,557$ configurations of the complex. We note that the deviation between *ab initio* and fitted values of dipole is substantially less than the accuracy of the dipole values obtained at our chosen CCSD(T)-F12a/aug-cc-pVTZ level of theory.

3.2. Dynamical equations

Let us introduce the generalized coordinates describing the position of moieties relative to the space-fixed frame of reference placed at the center of mass of the complex. Let $\mathbf{R} = (R, \Phi, \Theta)$ be the vector connecting the moieties' centers of mass and $\mathbf{r} = (r, \eta, \chi)$ be the vector oriented along N_2. The Hamiltonian of the N_2−Ar system breaks up into

$$H = K_{\text{tr}} + K_{\text{rot}} + K_{\text{int}} + U + V_1, \tag{10}$$

where U is the intermolecular potential, V_1 is the one-body energy of isolated N_2, and the translational, rotational and internal components of the kinetic energy are given by

$$\begin{aligned} K_{\text{tr}} &= \frac{p_R^2}{2\mu} + \frac{p_\Theta^2}{2\mu R^2} + \frac{p_\Phi^2}{2\mu R^2 \sin^2\Theta}, \\ K_{\text{rot}} &= \frac{p_\chi^2}{2I_1} + \frac{p_\eta^2}{2I_1 \sin^2\chi}, \\ K_{\text{int}} &= \frac{p_r^2}{2\mu_1}, \end{aligned} \tag{11}$$

respectively. Here, μ_1 and I_1 refer to the reduced mass and the inertia tensor of N_2, and μ is the reduced mass of the complex. The momentum conjugated to the generalized variable ξ is designated via p_ξ. The one-body potential V_1 was represented as a Morse curve:

$$V_1(r) = D_0\left[1 - \exp\left(-a(r - r_e)\right)\right], \quad a = 2\pi c \nu_0 \sqrt{\frac{\mu_1}{2D_0}}, \tag{12}$$

where $D_0 = 9.91$ eV is the dissociation limit and $\nu_0 = 2358.57$ cm^{-1} is the harmonic vibrational frequency.

The time-evolution of the complex is obtained from the solution of Hamilton equations of motion:

$$\begin{aligned} \dot{R} &= \frac{p_R}{\mu}, \\ \dot{p}_R &= \frac{p_\Theta^2}{\mu R^3} + \frac{p_\Phi^2}{\mu R^3 \sin^2\Theta} - \frac{\partial U}{\partial R}, \\ \dot{\Phi} &= \frac{p_\Phi}{\mu R^2 \sin^2\Theta}, \\ \dot{p}_\Phi &= -\frac{\partial U}{\partial \Phi}, \\ \dot{\Theta} &= \frac{p_\Theta}{\mu R^2}, \\ \dot{p}_\Theta &= \frac{p_\Phi^2 \cos\Theta}{\mu R^2 \sin^3\Theta} - \frac{\partial U}{\partial \Theta}, \\ \dot{r} &= \frac{p_r}{\mu_1}, \\ \dot{p}_r &= \frac{p_\chi^2}{\mu_1 r^3} + \frac{p_\eta^2}{\mu_1 r^3 \sin^2\chi} - \frac{\partial U}{\partial r} - \frac{\partial V_1}{\partial r}, \\ \dot{\eta} &= \frac{p_\eta}{I_1 \sin^2\chi}, \\ \dot{p}_\eta &= -\frac{\partial U}{\partial \eta}, \\ \dot{\chi} &= \frac{p_\chi}{I_1}, \\ \dot{p}_\chi &= \frac{p_\chi^2 \cos\chi}{I_1 \sin^3\chi} - \frac{\partial U}{\partial \chi}, \end{aligned} \tag{13}$$

where the momentum conjugated to the generalized variable ξ is represented by p_ξ.

To obtain the derivatives of the PIP-NN PES with respect to the generalized variables, the following formulas derived from the chain rule are employed:

$$\begin{bmatrix} \frac{\partial U}{\partial R} \\ \frac{\partial U}{\partial \Phi} \\ \frac{\partial U}{\partial \Theta} \end{bmatrix} = \begin{bmatrix} \cos\Phi\sin\Theta & \sin\Phi\sin\Theta & \cos\Theta \\ -R\sin\Phi\sin\Theta & R\cos\Phi\sin\Theta & 0 \\ R\cos\Phi\cos\Theta & R\sin\Phi\cos\Theta & -R\sin\Theta \end{bmatrix} \begin{bmatrix} \frac{\partial U}{\partial x_{\text{Ar}}} \\ \frac{\partial U}{\partial y_{\text{Ar}}} \\ \frac{\partial U}{\partial z_{\text{Ar}}} \end{bmatrix}, \tag{14}$$

$$\begin{aligned} \begin{bmatrix} \frac{\partial U}{\partial r} \\ \frac{\partial U}{\partial \eta} \\ \frac{\partial U}{\partial \chi} \end{bmatrix} = &\begin{bmatrix} \frac{1}{2}\cos\eta\sin\chi & \frac{1}{2}\sin\eta\sin\chi & \frac{1}{2}\cos\chi \\ -\frac{1}{2}r\sin\eta\sin\chi & \frac{1}{2}r\cos\eta\sin\chi & 0 \\ \frac{1}{2}r\cos\eta\cos\chi & \frac{1}{2}r\sin\eta\cos\chi & -\frac{1}{2}r\sin\chi \end{bmatrix} \begin{bmatrix} \frac{\partial U}{\partial x_{\text{N1}}} \\ \frac{\partial U}{\partial y_{\text{N1}}} \\ \frac{\partial U}{\partial z_{\text{N1}}} \end{bmatrix} + \\ &\begin{bmatrix} \frac{1}{2}\cos\eta\sin\chi & -\frac{1}{2}\sin\eta\sin\chi & -\frac{1}{2}\cos\chi \\ \frac{1}{2}r\sin\eta\sin\chi & -\frac{1}{2}r\cos\eta\sin\chi & 0 \\ -\frac{1}{2}r\cos\eta\cos\chi & -\frac{1}{2}r\sin\eta\cos\chi & \frac{1}{2}r\sin\chi \end{bmatrix} \begin{bmatrix} \frac{\partial U}{\partial x_{\text{N2}}} \\ \frac{\partial U}{\partial y_{\text{N2}}} \\ \frac{\partial U}{\partial z_{\text{N2}}} \end{bmatrix}. \end{aligned} \tag{15}$$

3.3. Calculation of the correlation function

The dipole time-correlation function is calculated directly using the Monte Carlo approach based on an ensemble of trajectories emerging from statistically sampled initial conditions. The sampling of initial conditions from the Boltzmann density ρ is performed using the rejection scheme. The algorithm utilizes the proposal distribution

$$\rho_0(\mathbf{q}, \mathbf{p}) = \exp\left(-\frac{K_{\text{tr}} + K_{\text{rot}} + K_{\text{int}}}{k_{\text{B}}T}\right) \tag{16}$$

selected such that it envelopes the target distribution over the support

$$\rho(\mathbf{q}, \mathbf{p}) \leqslant W \rho_0(\mathbf{q}, \mathbf{p}), \tag{17}$$

where W is a constant. Note that the sum $U + V_1$ is bounded from below, whereas the term U alone may be unbounded. This allows us to construct the rejection scheme as described in [10] with the intermolecular potential U replaced with the sum $U + V_1$.

3.4. Comparison with the experiment

The spectral function $G(\nu)$ is given by the Fourier transform of the time-correlation function:

$$G(\nu) = \frac{1}{2\pi}\int_{-\infty}^{+\infty} C(t) e^{-2\pi i c \nu t}\, \mathrm{d}t, \tag{18}$$

where ν is the frequency in cm^{-1}. The absorption coefficient $\alpha(\nu)$ is obtained by multiplication of the spectral function $G(\nu)$ by the radiation term common for all the absorbers [30]

$$\alpha(\nu) = \frac{(2\pi)^4 N_L^2}{3hc}\nu\left(1 - \exp\left(-\frac{hc\nu}{k_{\text{B}}T}\right)\right) G(\nu), \tag{19}$$

where N_L is the Loschmidt number.

The classical lineshape provided by Eq. (18) has to be corrected to satisfy the detailed balance condition prior to be compared to the experimentally measured profiles. Bader and Berne [31] demonstrated that in the case, where the classical and quantum systems are characterized by the same effective harmonic Hamiltonian and the dipole moment function can be written as a combination of the effective normal modes of the system, the classical $G_{\text{cl}}(\nu)$ and quantum $G_{\text{q}}(\nu)$ line shapes are related by

$$G_{\text{q}}(\nu) = \frac{\beta h c \nu}{1 - \exp(-\beta h c \nu)} G_{\text{cl}}(\nu), \tag{20}$$

where $\beta = (k_B T)^{-1}$ is the reciprocal temperature in units of energy. It can be easily shown that the desymmetrization given by Eq. (20) yields a spectral function that satisfies the detailed balance:

$$G_q(-\nu) = \frac{-\beta hc\nu}{1-\exp(\beta hc\nu)} G_{cl}(-\nu) = \frac{-\beta hc\nu}{1-\exp(\beta hc\nu)} G_{cl}(\nu) = \\ = \frac{-\beta hc\nu}{1-\exp(\beta hc\nu)} \frac{1-\exp(-\beta hc\nu)}{\beta hc\nu} G_q(\nu) = \exp(-\beta hc\nu) G_q(\nu) \quad (21)$$

The correction factor of Ref. [31] is shown to provide accurate results for adjusting vibrational IR amplitudes (e.g., see [32]). On the other hand, Schofield's procedure given by

$$G_{Sch}(\nu) = \exp\left(\frac{\beta hc\nu}{2}\right) G_{cl}(\nu), \quad (22)$$

has been shown to provide a satisfactory correction in the case of the CIA rototranslational bands (e.g., see [9,10]). Here, we utilize a combination of two quantum corrections to take into account the quantum balance. First, the procedure given by Eq. (20) is applied to the classical spectral function, and the produced maximum intensity of the fundamental band is noted. Next, we start with classical spectral function again and apply Schofield's correction (Eq. (22)) to both rototranslational and fundamental bands with respect to their band centers [30]. Finally, the maximum of the fundamental band is normalized using the value recorded in the first step.

We have to emphasize that any desymmetrization procedure is approximate. There is no known general recipe for correctly transforming a spectral profile from classical to quantum shape. Nevertheless, it is known that certain expressions recommended for spectral profile corrections perform better than others, depending on the nature of the spectral transitions, either rotational or vibrational. Based on our past experience with CIA spectra modeling, we aimed to combine the benefits of two widely used desymmetrization procedures. As we will see next, the result agrees satisfactorily with observations, indirectly supporting our chosen desymmetrization scheme.

Compared to the calculation utilizing the rigid-monomer approximation, the sampling rate needs to be increased since the intermolecular vibration is significantly faster than the softer intermolecular modes. Here, we employed a sampling rate of 1.2 fs. As a result of the inclusion of intermolecular vibration, we observed only a marginal decrease in the speed of trajectory propagation, at least for trajectories with energies that are probable at near-room temperature.

The comparison of the theoretical spectra with the experimental data in the far- and mid-infrared regions is presented in Figs. 6 and 7, respectively. The simulated profiles agree satisfactorily with the experimental ones for both bands corresponding to the range of the rototranslational and rovibrational fundamental bands of the N_2 molecule. The lower part of Fig. 6 shows the difference between the band spectra calculated for 300 K using the full-dimensional and reduced (assuming rigid monomers) interaction potentials. The difference is comparable to the residual Monte Carlo noise resulting from a simulation with 2 million trajectories, indicating that the rigid monomer approximation is well suited for such a collisional system.

Because of its stiffness, the N_2 vibrational mode is almost non-activated when performing a full-dimensional trajectory calculation at room temperature. Only the harmonic variation in the potential determines the position of the 1–0 CIA band. Consequently, the band center obtained in the classical trajectories calculation coincides with the harmonic frequency of the band (2358.5 cm^{-1}). From the quantum-mechanical perspective, the band center is shifted compared to the harmonic frequency by $\Delta = -2\nu_0\chi_0 = -\nu_0^2/(2D_0)$ if the N_2's internal potential is characterized by the Morse curve. Applying the parameters of Eq. (12) yields a shift of approximately 34 cm^{-1}. This estimate is in agreement with the shift, $\Delta = 28.58$ cm^{-1}, derived from the experimental data. The band center of the calculated spectrum in Fig. 7 is intentionally shifted to have it aligned with the observed band's maximum at 2392.92 cm^{-1}.

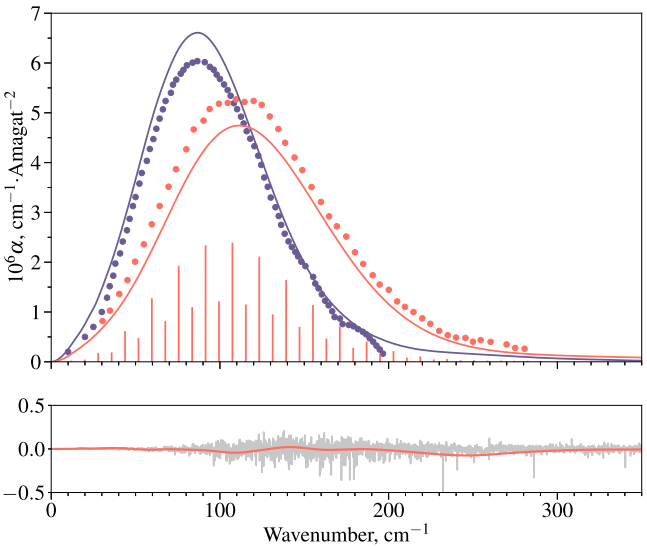

Fig. 6. Upper panel: N_2–Ar CIA spectra in the rototranslational band at 179 K (blue) and 300 K (red). Trajectory-based profiles are shown by the solid curves and the measurement data from Dore and Filabozzi [33] are represented by circles. Red vertical bars constitute a stick spectrum of the N_2 $S(J)$ transitions at 300 K. Lower panel: Difference between the 300-K band profiles calculated with the full-dimensional and reduced PES (red solid curve) in comparison with the typical numerical noise of the calculation method (shown by the gray area).

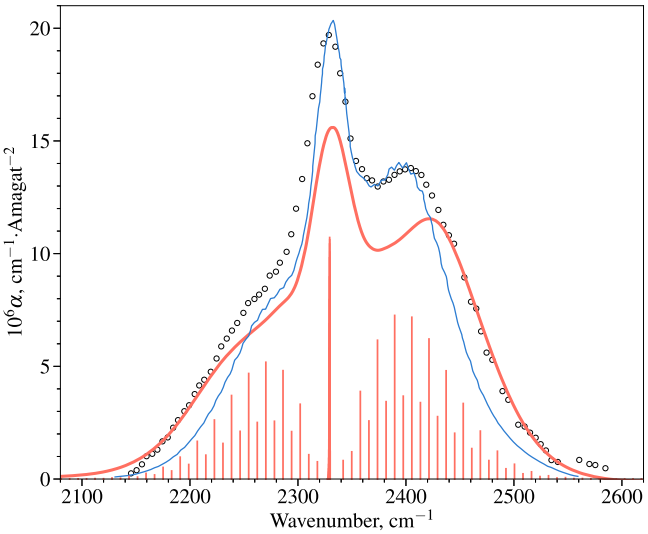

Fig. 7. N_2–Ar CIA spectra in the N_2 fundamental band region at 300 K. The trajectory-based profile is shown by the red thick solid line. The measured values from Moreau [34] and Buontempo et al. [35] are represented with the blue line and empty circles, respectively. The red vertical lines represent the discrete electric quadrupolar $O(J)$, $Q(J)$ and $S(J)$ transitions of nitrogen at 300 K.

Good agreement between the calculation results and the experimental data obtained in this work in the millimeter-wave range is demonstrated in Fig. 8. In this case, only spectral functions are shown because they give more information than absorption spectra. The experimental data (red points in Fig. 3) were averaged over 5 neighboring frequency points for comparison. In this frequency range under usual conditions the specific shape of the spectrum is stipulated mostly by free molecular pairs. However, at low temperatures the spectral feature corresponding to the rotation of the colliding pair as a whole may be revealed. To support this statement, in Fig. 8 we plot the diagram of the N_2–Ar rigid rotor transitions. The rightmost line in the diagram corresponds to the rotational dissociation limit of the dimer.

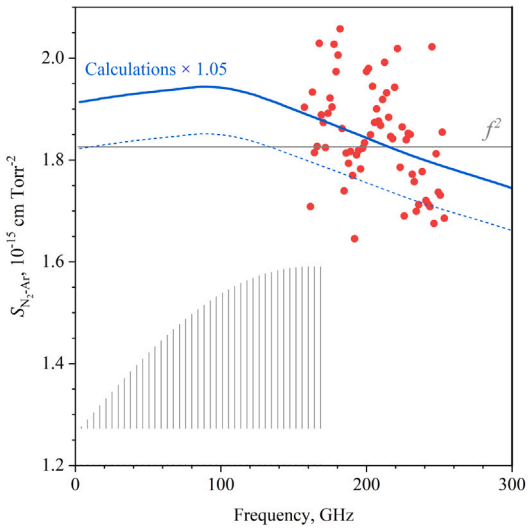

Fig. 8. N_2–Ar spectral function in the millimeter-wave range. Experimental data from Fig. 3 averaged over 5 neighbor frequencies are shown by red points. The CTS result is shown as is (dotted curve) and adjusted to the experimental data (multiplied by factor 1.05, thick solid curve). The thin horizontal line is for the quadratic with frequency function fitted to the experimental data. The vertical bars are the N_2–Ar rigid rotor spectrum stick-diagram (see text for details).

The numerical data on the equilibrium structure of the dimer and its dissociation energy from Hewage et al. [36] were used. The diagram suggests that the broad peak near 100 GHz in the spectral function should be attributed to the envelope of the rotational spectra of N_2–Ar dimer. Note that the N_2–N_2 dimer has similar rotational constants, leading to a similar peak in the N_2–N_2 spectral function (Fig. 4).

4. Comparison of the N_2–N_2 absorption models

In this section, we are going to compare our current model for N_2–N_2 absorption, which resulted from the combined experimental and theoretical CTS efforts, with previously published models. Two models were selected for the comparison: (i) the empirical quadratic with frequency model on the basis of the experimental data from [5]:

$$\alpha(\nu) = C_0 \left(\frac{300}{T}\right)^{n_0} \nu^2 p^2 \tag{23}$$

with $C_0 = 1.877(13) \times 10^{-18}$ cm^{-1}/(Torr^{2}GHz^2) and $n_0 = 3.27(7)$, and (ii) the dry air absorption model from the current MPM version [20] with the difference between dry air and nitrogen absorption taken into account though the efficiency factor $C_{\text{air}} = 0.84 C_{N_2-N_2}$, as suggested in [37]:

$$\alpha(\nu) = 0.5\ C_0 \left(\frac{300}{T}\right)^{n_0} \nu^2 p^2 \left(1 + \frac{1}{1 + (\nu/450)^2}\right) \tag{24}$$

with $C_0 = 2.105 \times 10^{-18}$ cm^{-1}/(Torr^{2}GHz^2), $n_0 = 3.22$.

The corresponding spectral functions can be compared with the present model in Figs. 2 and 4 demonstrating good quantitative agreement of all the models in the frequency and temperature range of the available experimental data (230–330 K). Fig. 9 shows that the spectral functions of these models differ significantly at 93 K, which is the typical surface temperature for Titan. Recall that the binary intermolecular interaction based models are still valid for the conditions of the Titan atmosphere.

We demonstrate the difference between the considered models by an example of calculation of brightness temperature of the Titan atmosphere, which is widely used in remote sensing for retrieval of the pressure or temperature profile from radiometric data. For this purpose, we used the PyRTLib program code [38], which allows calculating the brightness temperature of the atmosphere in the subTHz spectral range

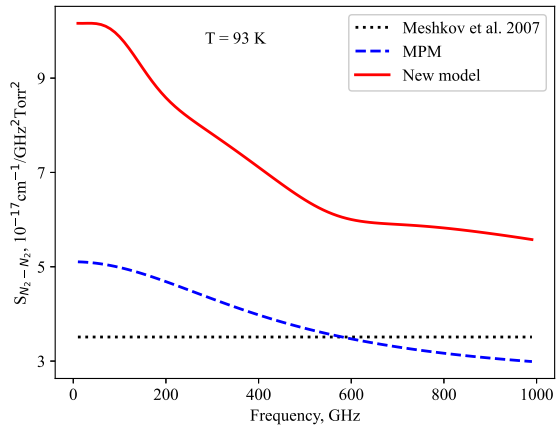

Fig. 9. N_2–N_2 spectral functions calculated for 93 K using the three considered models.

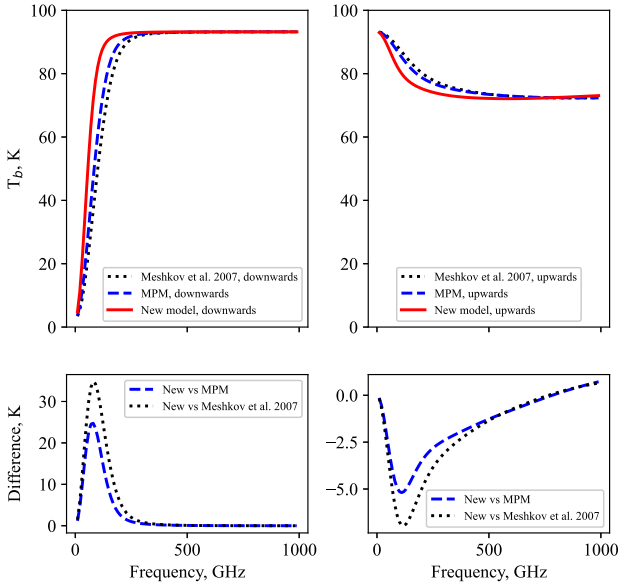

Fig. 10. Brightness temperature in the Titan atmosphere' SubTHz spectral domain as calculated according to different N_2–N_2 models (see the legend) for the upward (right) and downward (left) radiation flows (see text for details).

on the basis of any particular absorption model. The temperature and pressure profiles of the Titan atmosphere from [39,40] were used. For simplicity, the atmosphere was assumed to consist of pure nitrogen (the real content is about 94.2% of N_2, 5.7% of CH_4 and 0.1% of H_2).

Both upward (the radiometer is located on the top of the atmosphere) and downward (the radiometer is located on the surface of the planet) measurements directions were considered (Fig. 10).

The figure shows that in the millimeter-wave range the difference may be very significant, reaching from several to tens Kelvin depending on the frequency and method of observation. However, the atmosphere becomes opaque at the frequencies exceeding approximately 300 GHz, which leads to negligible differences between models.

5. Conclusions

The present paper extends both the experimental dataset and the level of the theoretical description of the bimolecular absorption in the N_2–N_2 and N_2–Ar collisional systems. The continuous spectra of N_2–N_2 were measured in an exceptionally broad spectral interval ranging from 77 up to 354 GHz. This feature allowed us to present the first reliable experimental demonstration of the theoretically predicted

deviation of the millimeter-wave continuum absorption in nitrogen from the frequency-squared dependence (Fig. 2). Very good agreement was found between the measured data (including the presently most accurate data from [5]) and those calculated by the CTS method N_2–N_2 spectra, as far as their frequency and temperature dependencies are concerned. The theoretical spectra slightly adjusted to better fit our new experimental data, allowed constructing the new broad-band practical model for the radiative transfer simulation in the sub-terahertz spectral range for the nitrogen-rich atmospheres at temperatures within 70–200 and 200–330 K. The model allowed us to retrieve the N_2–Ar continuum from the absorption measured in a mixture of nitrogen with argon (Fig. 3). These data together with the previously known experimental data in the far- and mid-infrared were used to confirm high reliability of the theoretical N_2–Ar spectra obtained by the CTS method. The full-dimensional PES and IDS were used in such calculations for the first time. This theoretical extension made it possible to calculate the shape of the N_2–Ar absorption band in the range of the N_2 molecule fundamental vibration (Fig. 7). The sufficiency of the rigid monomer assumption for the CTS simulation of the N_2–Ar rototranslational band (Fig. 6) was also demonstrated.

CRediT authorship contribution statement

E.A. Serov: Writing – original draft, Visualization, Validation, Formal analysis. **T.A. Galanina:** Validation, Methodology, Formal analysis, Data curation. **A.O. Koroleva:** Visualization, Investigation, Formal analysis. **D.S. Makarov:** Visualization, Software. **I.S. Amerkhanov:** Formal analysis, Data curation. **M.A. Koshelev:** Methodology, Formal analysis, Data curation. **M.Yu. Tretyakov:** Writing – review & editing, Supervision, Methodology. **D.N. Chistikov:** Software, Investigation, Data curation. **A.A. Finenko:** Writing – original draft, Visualization, Software, Investigation. **A.A. Vigasin:** Writing – review & editing, Methodology, Conceptualization.

Declaration of competing interest

There are no conflicts of interest to declare.

Data availability

Data will be made available on request.

Acknowledgments

The Russian Science Foundation (project No. 22-72-10118[1]) supported the study with the resonator spectrometer. The experimental part of the work was done using the research facilities “CKP-7” (USU №3589084). The CTS method was developed and used for spectral simulation by DNC, AAF, and AAV with partial support from the state assignment to A.M. Obukhov Institute of Atmospheric Physics RAS (FMWR-2022-0010 and FMWR-2022-0016).

Appendix A. Supplementary data

Supplementary material related to this article contains full-dimensional two-body PIP-NN models implemented in C/C++ for potential energy and induced dipole for N_2–Ar system.

Supplementary material related to this article can be found online at https://doi.org/10.1016/j.jqsrt.2024.109172.

[1] https://rscf.ru/en/project/22-72-10118/

References

[1] Trafton LM. Planetary atmospheres: The role of collision-induced absorption. In: Vigasin AA, Slanina Z, editors. molecular complexes in earth’s, planetery, cometary and interstellar atmospheres. World Scientific, London; 1998, p. 177–93.

[2] Koroleva AO, Odintsova TA, Tretyakov MYu, Pirali O, Campargue A. The foreign-continuum absorption of water vapour in the far-infrared (50–500 cm^{-1}). J Quant Spectrosc Radiat Transfer 2021;261:107486.

[3] Rinsland C, Zander R, Namkung J, Farmer C, Norton R. Stratospheric infrared continuum absorptions observed by the ATMOS instrument. J Geophys Res: Atmos 1989;94(D13):16303–22.

[4] Finenko AA, Bézard B, Gordon IE, Chistikov DN, Lokshtanov SE, Petrov SV, et al. Trajectory-based simulation of far-infrared collision-induced absorption profiles of CH_4-N_2 for modeling Titan’s atmosphere. Astrophys J Suppl Ser 2022;258(2):33. http://dx.doi.org/10.3847/1538-4365/ac36d3.

[5] Meshkov AI, De Lucia FC. Laboratory measurements of dry air atmospheric absorption with a millimeter wave cavity ringdown spectrometer. J Quant Spectrosc Radiat Transfer 2007;108(2):256–76.

[6] Serov EA, Balashov AA, Tretyakov MYu, Odintsova TA, Koshelev MA, Chistikov DN, et al. Continuum absorption of millimeter waves in nitrogen. J Quant Spectrosc Radiat Transfer 2020;242:106774.

[7] Karman T, Miliordos E, Hunt KL, Groenenboom GC, van der Avoird A. Quantum mechanical calculation of the collision-induced absorption spectra of N_2–N_2 with anisotropic interactions. J Chem Phys 2015;142(8).

[8] Bussery-Honvault B, Hartmann J-M. Ab initio calculations for the far infrared collision induced absorption by N_2 gas. J Chem Phys 2014;140(5).

[9] Chistikov DN, Finenko AA, Lokshtanov SE, Petrov SV, Vigasin AA. Simulation of collision-induced absorption spectra based on classical trajectories and ab initio potential and induced dipole surfaces. I. Case study of N_2-N_2 rototranslational band. J Chem Phys 2019;151(19):194106. http://dx.doi.org/10.1063/1.5125756.

[10] Chistikov DN, Finenko AA, Kalugina YN, Lokshtanov SE, Petrov SV, Vigasin AA. Simulation of collision-induced absorption spectra based on classical trajectories and ab initio potential and induced dipole surfaces. II. CO_2–Ar rototranslational band including true dimer contribution. J Chem Phys 2021;155(6):064301. http://dx.doi.org/10.1063/5.0060779.

[11] Gordon IE, Rothman LS, Hargreaves RJ, Hashemi R, Karlovets EV, Skinner FM, et al. The HITRAN2020 molecular spectroscopic database. J Quant Spectrosc Radiat Transfer 2022;277:107949.

[12] Liebe HJ. Atmospheric millimeter-wave propagation model. Int J Infrared Millim Waves 1989;10(6):631–50.

[13] Vigasin AA. Water vapor continuous absorption in various mixtures: Possible role of weakly bound complexes. J Quant Spectrosc Radiat Transfer 2000;64(1):25–40.

[14] Koshelev MA, Leonov II, Serov EA, Chernova AI, Balashov AA, Bubnov GM, et al. New frontiers in modern resonator spectroscopy. IEEE Trans Terahertz Sci Technol 2018;8(6):773–83.

[15] Serov EA, Parshin VV, Bubnov GM. Reflectivity of metals in the millimeter wavelength range at cryogenic temperatures. IEEE Trans Microw Theory Tech 2016;64:3828–38. http://dx.doi.org/10.1109/TMTT.2016.2609411.

[16] Koshelev MA, Serov EA, Parshin VV, Tretyakov MYu. Millimeter wave continuum absorption in moist nitrogen at temperatures 261–328 K. J Quant Spectrosc Radiat Transfer 2011;112:2704–12.

[17] Bauer A, Godon M, Carlier J, Gamache RR. Continuum in the windows of the water vapor spectrum. Absorption of H_2O–Ar at 239 GHz and linewidth calculations. J Quant Spectrosc Radiat Transfer 1998;59:273–85.

[18] Finenko AA. Accurate neural-network-based fitting of full-dimensional N_2–Ar and N_2–CH_4 two-body potential energy surfaces aimed at spectral simulations. Mol Phys 2024;e2348110. http://dx.doi.org/10.1080/00268976.2024.2348110.

[19] Rosenkranz PW. Line-by-line microwave radiative transfer (non-scattering. Rem Sens Code Lib 2017. http://dx.doi.org/10.21982/M81013.

[20] MWRnet - An international network of ground-based microwave radiometers. 2023, http://cetemps.aquila.infn.it/mwrnet/lblmrt_ns.html.

[21] Galanina TA, Koroleva AO, Amerkhanov IS, Serov EA, Koshelev MA, Tretyakov MYu, et al. On the nature of sub-THz continuum absorption in CO_2 gas, its mixture with Ar, and in pure water vapor. Phys Chem Chem Phys 2024;26:15032. http://dx.doi.org/10.1039/D4CP00240G.

[22] Jiang B, Guo H. Permutation invariant polynomial neural network approach to fitting potential energy surfaces. J Chem Phys 2013;139(5):054112. http://dx.doi.org/10.1063/1.4817187.

[23] Xie Z, Bowman JM. Permutationally invariant polynomial basis for molecular energy surface fitting via monomial symmetrization. J Chem Theory Comput 2010;6(1):26–34. http://dx.doi.org/10.1021/ct9004917.

[24] Xie Z, Bowman JM. https://github.com/Kee-Wang/PES-Fitting-MSA. [Online; Accessed 17 July 2023].

[25] Paukku Y, Yang KR, Varga Z, Truhlar DG. Global ab initio ground-state potential energy surface of N_4. J Chem Phys 2013;139(4):044309. http://dx.doi.org/10.1063/1.4811653.

[26] Braams BJ, Bowman JM. Permutationally invariant potential energy surfaces in high dimensionality. Int Rev Phys Chem 2009;28(4):577–606. http://dx.doi.org/10.1080/01442350903234923.

[27] Werner H-J, Knowles PJ, Knizia G, Manby FR, Schütz M, Celani P, et al. MOLPRO, version 2010.1, a package of *ab initio* programs, See http://www.molpro.net.

[28] Boys SF, Bernardi F. The calculation of small molecular interactions by the differences of separate total energies. Some procedures with reduced errors. Mol Phys 1970;19(4):553–66. http://dx.doi.org/10.1080/00268977000101561.

[29] Bendtsen J, Rasmussen F. High-resolution incoherent Fourier transform Raman spectrum of the fundamental band of $^{14}N_2$. J Raman Spectrosc 2000;31(5):433–8. http://dx.doi.org/10.1002/1097-4555(200005)31:5<433::AID-JRS554>3.3.CO;2-K.

[30] Frommhold L. Collision induced absorption in gases. Cambridge: Cambridge University Press; 2006.

[31] Bader JS, Berne BJ. Quantum and classical relaxation rates from classical simulations. J Chem Phys 1994;100(11):8359–66. http://dx.doi.org/10.1063/1.466780.

[32] Gaigeot M-P, Sprik M. Ab initio molecular dynamics computation of the infrared spectrum of aqueous uracil. J Phys Chem B 2003;107(38):10344–58. http://dx.doi.org/10.1021/jp034788u.

[33] Dore P, Filabozzi A. On the nitrogen-induced far-infrared absorption spectra. Can J Phys 1987;65:90–3. http://dx.doi.org/10.1139/p87-016.

[34] Moreau G. Étude en température et modélisation de l'absorption induite par collision dans les régions des bandes fondamentales pour les mélanges des gaz N_2 et O_2 [Ph.D. thesis], Université de Rennes; 1999.

[35] Buontempo U, Filabozzi A, Maselli P. Collision induced fundamental band of N_2 and N_2–Ar mixtures. Mol Phys 1989;67(3):517–23. http://dx.doi.org/10.1080/00268978900101261.

[36] Hewage JW, Amar FG, de Feraudy M-F, Torchet G. The structure of mixed nitrogen-argon clusters: A comparison of simulation results with experimental electron diffraction patterns. Eur Phys J D 2003;24:249–52. http://dx.doi.org/10.1140/epjd/e2003-00148-y.

[37] Boissoles J, Boulet C, Tipping RH, Brown A, Ma Q. Theoretical calculation of the translation-rotation collision-induced absorption in N_2–N_2, O_2–O_2, and N_2–O_2 pairs. J Quant Specrosc Radiat Transfer 2003;82:505–16. http://dx.doi.org/10.1016/S0022-4073(03)00174-2.

[38] Larosa S, Cimini D, Gallucci D, Nilo S, Romano F. PyRTlib: An educational Python-based library for non-scattering atmospheric microwave radiative transfer computations. Geosci Model Dev 2024;17:2053–76. http://dx.doi.org/10.5194/gmd-17-2053-2024.

[39] Hörst SM. Titan's atmosphere and climate. J Geophys Res: Planets 2017;122. http://dx.doi.org/10.1002/2016JE005240.

[40] Lyne J, Ramsey P. Investigation of Titan aerogravity assist for capture into orbit about saturn. J Spacecr Rockets 2006;43:231–3. http://dx.doi.org/10.2514/1.9274.